Icarus 206 (2010) 561–572

Contents lists available at ScienceDirect

Icarus

journal homepage: www.elsevier.com/locate/icarus

Carbon dioxide on the satellites of Saturn: Results from the *Cassini* VIMS investigation and revisions to the VIMS wavelength scale

Dale P. Cruikshank [a,*], Allan W. Meyer [b], Robert H. Brown [c], Roger N. Clark [d], Ralf Jaumann [e], Katrin Stephan [e], Charles A. Hibbitts [f], Scott A. Sandford [a], Rachel M.E. Mastrapa [a], Gianrico Filacchione [g], Cristina M. Dalle Ore [h], Philip D. Nicholson [i], Bonnie J. Buratti [j], Thomas B. McCord [k], Robert M. Nelson [j], J. Brad Dalton [j], Kevin H. Baines [j], Dennis L. Matson [j]

[a] *NASA Ames Research Center, Mail Stop 245-6, Moffett Field, CA 94035-1000, USA*
[b] *USRA, NASA Ames Research Center, Moffett Field, CA 94035-1000, USA*
[c] *Lunar and Planetary Lab., University of Arizona, Tucson, AZ 85721, USA*
[d] *U.S. Geological Survey, Mail Stop 964, Box 25046, Denver Federal Center, Denver, CO 80225, USA*
[e] *German Aerospace Center (DLR), Institute of Space Sensor Technology and Planetary Exploration, Rutherfordstrasse 2, D-12489 Berlin, Germany*
[f] *JHU-APL, 11100 Johns Hopkins Rd., Laurel, MD 20723, USA*
[g] *INAF-IASF via del Fosso del Cavaliere, 100, 00133 Roma, Italy*
[h] *SETI Institute, 515 N., Whisman Rd., Mountain View, CA 94043, USA*
[i] *Cornell University, 418 Space Sciences Building, Ithaca, NY 14853, USA*
[j] *Jet Propulsion Laboratory, 4800 Oak Grove Drive, Pasadena, CA 91109, USA*
[k] *Bear Fight Center, P.O. Box 667, Winthrop, WA 98862, USA*

ARTICLE INFO

Article history:
Received 27 February 2009
Revised 11 May 2009
Accepted 8 July 2009
Available online 17 July 2009

Keywords:
Saturn
Ices

ABSTRACT

Several of the icy satellites of Saturn show the spectroscopic signature of the asymmetric stretching mode of C–O in carbon dioxide (CO_2) at or near the nominal solid-phase laboratory wavelength of 4.2675 μm (2343.3 cm^{-1}), discovered with the Visible-Infrared Mapping Spectrometer (VIMS) on the Cassini spacecraft. We report here on an analysis of the variation in wavelength and width of the CO_2 absorption band in the spectra of Phoebe, Iapetus, Hyperion, and Dione. Comparisons are made to laboratory spectra of pure CO_2, CO_2 clathrates, ternary mixtures of CO_2 with other volatiles, implanted and adsorbed CO_2 in non-volatile materials, and ab initio theoretical calculations of $CO_2 * nH_2O$. At the wavelength resolution of VIMS, the CO_2 on Phoebe is indistinguishable from pure CO_2 ice (each molecule's nearby neighbors are also CO_2) or type II clathrate of CO_2 in H_2O. In contrast, the CO_2 band on Iapetus, Hyperion, and Dione is shifted to shorter wavelengths (typically ~4.255 μm (~2350.2 cm^{-1})) and broadened. These wavelengths are characteristic of complexes of CO_2 with different near-neighbor molecules that are encountered in other volatile mixtures such as with H_2O and CH_3OH, and non-volatile host materials like silicates, some clays, and zeolites. We suggest that Phoebe's CO_2 is native to the body as part of the initial inventory of condensates and now exposed on the surface, while CO_2 on the other three satellites results at least in part from particle or UV irradiation of native H_2O plus a source of C, implantation or accretion from external sources, or redistribution of native CO_2 from the interior.

The analysis presented here depends on an accurate VIMS wavelength scale. In preparation for this work, the baseline wavelength calibration for the Cassini VIMS was found to be distorted around 4.3 μm, apparently as a consequence of telluric CO_2 gas absorption in the pre-launch calibration. The effect can be reproduced by convolving a sequence of model detector response profiles with a deep atmospheric CO_2 absorption profile, producing distorted detector profile shapes and shifted central positions. In a laboratory blackbody spectrum used for radiance calibration, close examination of the CO_2 absorption profile shows a similar deviation from that expected from a model. These modeled effects appear to be sufficient to explain the distortion in the existing wavelength calibration now in use. A modification to the wavelength calibration for 13 adjacent bands is provided. The affected channels span about 0.2 μm centered on 4.28 μm. The maximum wavelength change is about 10 nm toward longer wavelength. This adjustment has implications for interpretation of some of the spectral features observed in the affected wavelength interval, such as from CO_2, as discussed in this paper.

Published by Elsevier Inc.

* Corresponding author.
E-mail address: dale.p.cruikshank@nasa.gov (D.P. Cruikshank).

0019-1035/$ - see front matter Published by Elsevier Inc.
doi:10.1016/j.icarus.2009.07.012

1. Introduction

The spectral absorption band of pure carbon dioxide in a solid state, nominally centered at 4.2675 μm (2343.3 cm^{-1}) [which we round to 4.268 μm herein] was discovered in the spectra of Saturn's satellites by the Visible-Infrared Mapping Spectrometer (VIMS) aboard the *Cassini* orbiting spacecraft, beginning with the in-bound encounter with Phoebe (Clark et al., 2005). It was subsequently found in the spectrum of Iapetus (Buratti et al., 2005) and then several other satellites (Brown et al., 2005; Clark et al., 2008). This band is invisible from ground-based telescopes because of the interference of terrestrial CO_2 gas in the atmosphere. Weaker bands of CO_2 ice near 2.0 μm have been found in the spectra of Triton (Cruikshank et al., 1993) and three satellites of Uranus (Grundy et al., 2006), while the *Galileo* NIMS data have revealed the 4.268-μm band in some regions of the surfaces of jovian satellites Ganymede and Callisto, although at slightly shifted wavelengths (McCord et al., 1998; Hibbitts et al., 2000; Hibbitts et al., 2002, 2003). Those shifted wavelengths suggested to McCord et al. and Hibbitts et al. (same references plus Hibbitts and Szanyi, 2007) that CO_2 may be complexed at the molecular level with other materials present on the satellite surfaces.

The importance of CO_2 on the Saturn and Jupiter satellites arises in part from its probable occurrence in the original condensates from which the satellites were formed (e.g., review by Estrada et al., in press). In addition, it is important because its long-term instability in pure condensed form at the mean surface temperatures of both of these satellite systems (e.g., Lebofsky, 1975; Palmer and Brown 2006; Palmer and Brown, 2008) indicates that special conditions of its formation and retention exist. The elucidation of those conditions may give useful insight into the circum-Saturn environment and processes on small Solar System bodies at nearly 10 AU distance from the Sun.

Carbon dioxide is also important in a chemical sense, providing a gateway to the formation of both simple and complex organic molecules (Delitsky and Lane, 2002).

As the CO_2 band was identified in other satellites of Saturn in the prime phase of the orbital tour, it was noted that the central wavelength and the profile of the band varied from satellite to satellite, and in some cases also locally across the surface of a given satellite (Stephan et al., in press; Clark et al., submitted for publication). In nearly every case, the central wavelength was found to be different from that measured in the laboratory for pure CO_2 ice at temperatures relevant to the satellites of Saturn, vis. 4.268 μm as noted above (Ehrenfreund et al., 1996, 1999; Sandford and Allamandola, 1990).

The variations from the laboratory wavelength of pure CO_2 prompted a study of the VIMS instrumental wavelength calibration in the region of the CO_2 band. The overall calibration of the instrument's wavelength scale was undertaken before launch (Brown et al., 2004) and then revised after in-flight spectrum measurements of celestial sources (McCord et al., 2004) by a uniform shift amounting to one VIMS channel, or ~0.017 μm in wavelength. In the course of the new investigation of the wavelength scale in the region of the CO_2 band (4.20–4.40 μm), the details of which are related below, we found a nonlinear distortion of the scale that we attribute to the original calibration measurements in the laboratory before launch.

2. Cassini VIMS wavelength calibration in the region 4.20–4.40 μm

Before discussing the detailed nature of CO_2 on Saturn's satellites, we introduce the matter of a small change to the wavelength calibration of the VIMS instrument in the spectral region centered on the 4.268-μm band, because accurate wavelength calibration is essential to understanding the variations of the band position seen in the satellite spectra.

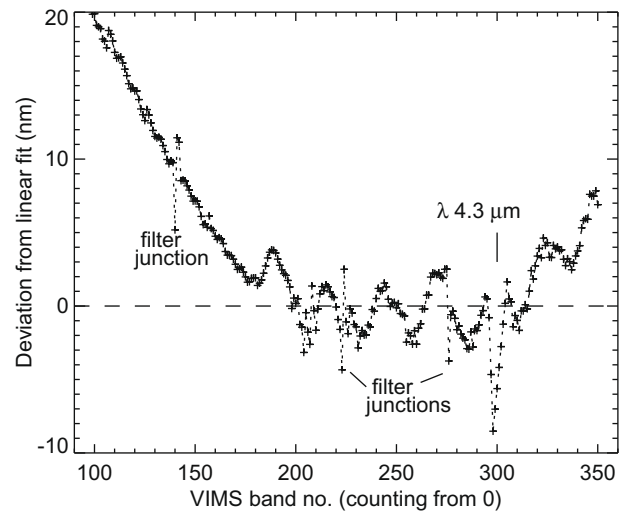

Fig. 1. Residuals from linear dispersion. The ordinate shows the deviations (in nm) of current VIMS baseline wavelength calibration RC15 from a least squares linear fit (Eq. (1)). Note the distinctive V-shaped downward deviation centered near band 300, or about 4.3 μm.

The VIMS has been described in detail elsewhere (Brown et al., 2004); briefly it provides data cubes with up to 64 × 64 pixels in the spatial field of view, and for each of these pixels 352 spectral channels, spanning a wavelength range of 0.35–5.1 μm. The visible-wavelength portion of the data cube is provided by a frame-transfer CCD. The infrared spectrum beyond 0.9 μm is provided by a single linear array of 256 InSb photo detectors with constant 0.12 mm spacing. The VIMS optics includes a tip/tilt mirror that step-scans the image plane over the entrance aperture of the IR spectrometer.

A plot of the current baseline VIMS IR wavelength values versus band number (denoted the "RC15" calibration[1]) are approximately linear. However, subtracting a least squares linear fit

$$\lambda = 0.01668 * B - 0.7381\ \mu m \quad \text{where } B : 96\text{–}351 \tag{1}$$

from the RC15 wavelength list leaves a small but definite pattern of residual deviations from linearity (Fig. 1).

Small deviations from linearity are not unexpected because of the complex optical path of the instrument and special characteristics of the VIMS diffraction grating, which has a triple blaze. In addition, several very narrow spikes (1–3 channels wide) occur at known positions of bandpass filter junctions, i.e. channels 140, 223, and 275. The deviation of interest here is the peculiar, "V"-shaped spike for bands 296–304 (4.20–4.33 μm), extending down to 9 nm deviation below the linear fit. The identification and interpretation of some spectral features observed in the Saturn system in this wavelength range are sensitive to their precise position and shape, so the reality and nature of even small deviations from fixed linear dispersion in this wavelength interval need to be accurately known. In the present paper, we consider only the abrupt and distinctive variation in the wavelength scale in the immediate region of the CO_2 band at 4.268 μm, but where other residuals in the dispersion linearity occur, possible deviations of the wavelength scale induced by telluric H_2O vapor in the calibration optical path might

[1] RC15 has subsequently been replaced by a new calibration file called RC17, which changes only the radiometric profile of the spectrometer's spectral response and does not affect the wavelength scale.

be explored. We note, however, that the other deviations seen in Fig. 1 are somewhat smaller than the maximum correction in this paper, which was 8.5 nm (Table 2), or about half a channel width.

We defer the details of the calibration investigation and methods of adjustment to the wavelength scale in the region of the CO_2 band to Appendix A, and summarize the basic results here.

The pre-launch calibration of the flight model VIMS was accomplished with the instrument in a thermal vacuum environment chamber at the Jet Propulsion Laboratory. For the wavelength calibration measurements, the VIMS itself was operated inside the evacuated chamber, but the source monochrometer was outside in ambient lab atmosphere (Brown et al., 2004, section 6.3). Although the source monochrometer output aperture was in close proximity to the chamber optical window, the total light path from the source lamp inside the monochrometer to the vacuum chamber window included about two meters of laboratory air. Detector response profiles were compiled by obtaining VIMS spectra while the monochrometer was tuned incrementally at 1 nm intervals through the full 1–5 μm VIMS spectral range. Upon conclusion of the calibration activities, it was noted that atmospheric absorption had strongly diminished the flux received by VIMS for several channels (bands) spanning the CO_2 gas band at ~4.3 μm. The central wavelength values for some of the affected bands were assigned by linear interpolation.

The resulting character of the wavelength calibration can be seen in Fig. 1, where the wavelength values for the affected bands are all shifted blueward by as much as about 10 nm, relative to what might have been obtained by just interpolating across the affected interval, or from the general linear fit to all of the IR detector scans. This distortion is evident to some degree for at least ten of the VIMS channels spanning the relatively broad CO_2 gas absorption band, beginning in channel 295 and extending through channel 307.

When a profile of atmospheric CO_2 gas absorption is convolved with an instrumental model consisting of a uniformly spaced sequence of VIMS response profiles at and around 4.3 μm, the character of the residuals from linearity in the RC15 wavelength scale is accurately reproduced. The new re-analysis of the calibration data reported here finds that the "V"-shaped feature in the deviations from linearity can be entirely explained by profile distortions introduced by the atmospheric absorption, and the accompanying interpolated values that were assigned to some of the affected bands. This explanation for the peculiar V-shaped wavelength deviation feature was independently confirmed by a separate investigation by one of us (Hibbitts) of the shape of the telluric CO_2 absorption feature present in a VIMS spectrum of a thermal continuum source, originally obtained as part of the pre-launch radiometric calibration activities. This additional evidence is also described further in the Appendix A.

In the absence of spectral features on the target objects (satellites, planet, rings) in this narrow wavelength range affected by the calibration procedure, the distortion could be ignored and might have gone unnoticed. However, because the relatively narrow absorption band of the CO_2 molecule has been detected on several of the satellites (as shown in Fig. 2), and because the central wavelength of this feature (and the band profile) varies from one object to another, as well as spatially across a given satellite, a rigorous investigation and clarification of the wavelength scale became necessary. The original pre-launch wavelength calibration data were obtained and re-analyzed, and new spectral response profiles for the affected bands were computed, corrected for telluric transmission. The revised central wavelengths for channels 295 through 307, listed in Table 2 have been used to adjust the CO_2 band data for each source on which it has been found, and the revised band positions and profiles, and their interpretation, are the subject of the present paper (see Fig. 2a).

Table 1
CO_2 bands on Saturn's satellites.

Satellite	Date	Region	λ_c (μm)	FWHM (nm)	Band depth (% of continuum)
Iapetus	2004 December 30–31	Low-albedo region	4.266	40.2	31
Iapetus	2007 September 10	98 lowest albedo px	4.263	44.5	33
Iapetus	2007 September 10	Low-albedo side mosaic	4.255	52.0	44
Hyperion	2005 September 25–26	Strongest CO_2 regions	4.253	41.4	39
Phoebe	2004 June 11	10,838 pixels, full image	4.266	24.4	19
Dione	2005 October 11	Trailing hemisphere	4.252	48.9	10

Table 2
Wavelength alternatives for 4.2 μm $\leqslant \lambda \leqslant$ 4.4 μm.

VIMS band #	RC15 baseline (μm)	RC15 deviations (nm)	Linear interp.	2nd order	Deconv. smooth	New (μm)
291	4.1145	−1.3		−0.7		4.1145
292	4.1318	−0.6		−0.6		4.1318
293	4.1488	−0.3		−0.5		4.1488
294	4.1664	+0.6		−0.5		4.1664
295	4.1830	+0.5	+0.5	−0.4	+0.7	**4.1832**
296	4.1984	−0.8	+0.6	−0.4	+0.9	**4.2001**
297	4.2112	−4.7	+0.7	−0.3	+1.1	**4.2170**
298	4.2240	−8.5	+0.8	−0.2	+1.2	**4.2337**
299	4.2422	−7.0	+0.9	−0.1	+1.3	**4.2505**
300	4.2603	−5.6	+1.1	−0.1	+1.4	**4.2673**
301	4.2784	−4.2	+1.2	−0.0	+1.4	**4.2840**
302	4.2965	−2.8	+1.3	+0.1	+1.3	**4.3006**
303	4.3147	−1.2	+1.4	+0.2	+1.2	**4.3171**
304	4.3328	+0.2	+1.5	+0.2	+1.0	**4.3336**
305	4.3509	+1.6	+1.6	+0.3	+0.9	**4.3502**
306	4.3665	+0.5		+0.4	+0.5	**4.3665**
307	4.3830	+0.3		+0.5	+0.2	**4.3829**
308	4.3979	−1.4		+0.6		4.3979

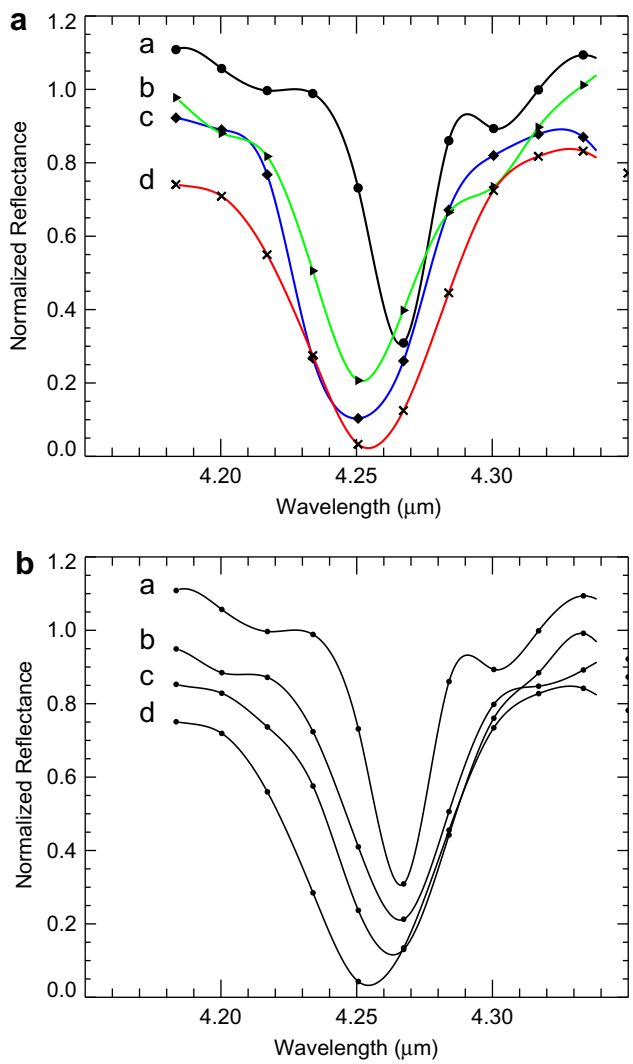

Fig. 2. (a) The CO_2 band on four of Saturn's satellites: (a) Phoebe, (b) Hyperion, (c) Dione, and (d) Iapetus (2007 data, 2440 dark pixels from mosaic of low-albedo hemisphere). See Table 1. These data have all been normalized to show similar band depth and offset vertically, and thus demonstrate differences in band width and central wavelength. The dots are the individual data points. The original Phoebe spectrum had a significant continuum slope, which was removed by fitting a 3rd degree polynomial to six points: $\lambda = 4.14883$, 4.1823, 4.2840, 4.335, 4.41537, and 4.4824 μm. A cubic spline interpolation was used to connect the data points for all four spectra. (b) The CO_2 band on Phoebe (a) and the low-albedo hemisphere of Iapetus taken from three separate data extractions: (b) 3226 pixels from the December 2004 fly-by, (c) the 98 pixels of lowest albedo and minimum H_2O contamination from the September, 2007 fly-by, and (d) 2440 pixels from the mosaic of the low-albedo hemisphere (see Jaumann et al., 2006) from the September, 2007 fly-by. See Table 1. These data have all been normalized to show similar band depth and offset vertically, and thus demonstrate differences in band width and central wavelength. The dots are the individual data points. The Phoebe spectrum was continuum-flattened as described in the caption to (a). A cubic spline interpolation was used to connect the data points for all four spectra.

3. CO_2 in spectra of Saturn's satellites

As noted by Clark et al. (2008), the CO_2 band is prominent in the spectra of Phoebe, Iapetus, Hyperion, and Dione, while it is seen weakly in the spectra of Mimas, Rhea, and Tethys. The exact wavelength and band profile of the (nominally) 4.268-μm asymmetric stretching mode of the linear CO_2 molecule is dependent on temperature and on the association of CO_2 molecules with others of the same or different kinds (e.g., Sandford and Allamandola, 1990, Fig. 3). In the present discussion we ignore gaseous and liquid CO_2, and consider only occurrences of CO_2 in the solid state, either as a pure substance or as a complex with other molecular species. On satellite surfaces dominated by H_2O ice, the reflectance is high at visible wavelengths but low in the 4-μm spectral region, in contrast to H_2O-poor satellite surfaces in which the visual reflectance is high but the reflectance around 4 μm is high, thus enabling the detection of CO_2 when present.

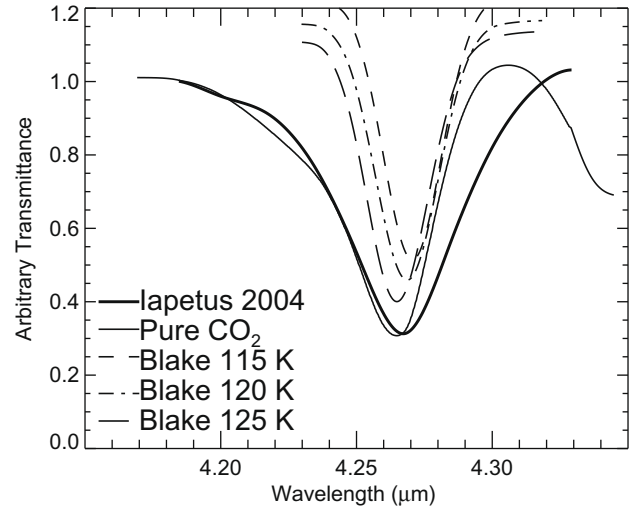

Fig. 3. The Iapetus 2004 CO_2 band is shown with the Sandford and Allamandola (1990) pure CO_2 (in transmission) and the Blake et al. (1991) type 2 CO_2 clathrate in H_2O and CH_3OH (H_2O:CO_2:CH_3OH = 100:50:1) at three different temperatures. The laboratory data have been convolved to the VIMS spectral resolution, $\lambda/\Delta\lambda = 255$; see footnote to text.

Table 1 summarizes the information we have obtained on the CO_2 absorption band in four of Saturn's satellites where it is seen most prominently, with the measured central wavelength and the full-width at half-maximum (FWHM) absorption in the band. We also show the depth of the CO_2 band as a percentage of the continuum value above zero, since this information is lost in the scaling and normalization in the figures and discussion below. The CO_2 absorption band in laboratory spectra is intrinsically narrower than the wavelength resolution of VIMS. In the region around 4.3 μm the individual detector elements are spaced 16.7 nm apart, center-to-center. Thus the intrinsic instrumental resolution is $\lambda/\Delta\lambda = 255$. Data sets for four satellites are plotted in Fig. 2a and b, demonstrating the similarities and differences among the data in terms of central wavelength, band profile, and band width of the CO_2 absorption band. We consider each satellite and each data set separately.

Standard error bars are not shown for the VIMS data in Fig. 2a and b because they are evaluated differently for each spectrum. Variance in the intensity of an individual spectral pixel averaged over several image cubes is usually dominated by image-to-image intensity differences, and to calculate a true standard deviation requires that each cube is normalized, a process that is not normally done in spectral processing. In the data above, the equivalent of a standard deviation in each spectral point that would contribute to an uncertainty in band profile for (a) Phoebe is $\leqslant$1%, for (b) Hyperion ~5%, for (c) Dione ~5%, for (d) Iapetus ~1%. For large numbers of pixels averaged, noise is usually smaller than the line width and scatter in the points is dominated by residual calibration errors and possible real spectral structure.

3.1. Phoebe

As Cassini entered the Saturn system, its first satellite encounter was with Phoebe. Clark et al. (2005) described the spectrum in

detail, reporting the discovery of CO_2 and the presence of H_2O ice that had been seen less well in earlier ground-based telescopic spectra. Taking essentially all of the VIMS spatial pixels covering Phoebe, (numbering 10,838), we have derived the average CO_2 band appearance, as shown in Fig. 2a. In a subsequent study, Coradini et al. (2008) used the G-mode statistical tool (Gavrishin et al., 1992) to classify regions of Phoebe's surface on the basis of band strengths of H_2O and various other parameters. They found that CO_2 band strength is more spatially variable across Phoebe than is the H_2O ice absorption band. Some regions show correlation of CO_2 with H_2O ice, as in the region around crater Erginus (diameter ~38 km, having bright landslips in exposed crater walls), while in some other regions the CO_2 band strength is anti-correlated with the absorption band at 2.42 μm that was originally thought to arise from CN compounds (Clark et al., 2005). Phoebe's CO_2 band shown in Fig. 2a has a central wavelength 4.266 μm, which is sensibly the same as the wavelength of pure CO_2 in the laboratory (see below).

3.2. Iapetus

Chronologically, CO_2 was next found in the surface materials of Iapetus during the first close fly-by in late December, 2004. The band is visible almost exclusively in the low-albedo material that coats the leading hemisphere of the body (Buratti et al., 2005). Using improved data (higher spatial resolution greater global coverage, and higher signal precision) obtained at the close fly-by of September 2007, Clark et al. (submitted for publication) have mapped the distribution of CO_2, noting that the central wavelength and strength of the band vary across the surface. The analysis presented here confirms the variability noted by Clark et al., and demonstrates this effect in Fig. 2b.

3.3. Hyperion

The surface of Hyperion is unique in the Saturn system, with large expanses of high-albedo H_2O ice and pockets of low-albedo material lying mostly in the bottoms of cup-shaped craters that differ in morphology from normal impact craters formed in a dense solid body. The unusual morphology of Hyperion's craters is interpreted by Thomas et al. (2007) as the result of impacts in an underdense, porous body; the density of Hyperion determined from mass and volume measurements is 0.54 ± 0.05 g cm^{-3} (Thomas et al., 2007). The CO_2 band is distributed in both low- and high-albedo material; a single patch of high CO_2 concentration can cross a boundary between these two kinds of material, or can be locally confined by albedo boundaries, as shown in compositional maps (Cruikshank et al., 2007). CO_2 is highly correlated with H_2O, and in contrast to Phoebe, in some regions it is correlated with the 2.42-μm absorption band.

The CO_2 band on Hyperion is distinguished by its breadth and the shift of its central wavelength toward shorter wavelengths, as seen in Fig. 2a. The band profile is also unique among the four satellites considered here, being not only broad, but somewhat bowl-shaped.

3.4. Dione

In terms of composition, Dione's surface is entirely dominated by high-albedo H_2O ice, with regions of the trailing hemisphere having a slightly lower albedo and a weakly brownish color. The spectral band of CO_2 is generally weak and distributed non-uniformly on Dione, being mostly concentrated in the discolored material on the trailing hemisphere in the region near 300°W (Clark et al., 2008; Stephan et al., in press).

4. CO_2 in the Solar System

4.1. Ices and clathrates

Carbon dioxide in a solid state is found in several astrophysical environments and on Solar System bodies from Mars to Triton. It can occur for astronomical timescales in the form of pure CO_2 ice and in mixtures with other frozen volatiles when the temperature is sufficiently low. In astrophysical sources (interstellar ices, circumstellar debris disks, etc.) the wavelength and band profile of the asymmetric stretching mode are known to vary from the nominal laboratory values for pure CO_2 if it occurs as a molecular mixture with polar (e.g., H_2O, CH_3OH) and non-polar (e.g., CO, O_2, CO_2 itself) molecules (e.g., Sandford and Allamandola, 1990; Ehrenfreund et al., 1999; Gerakines et al., 1999). CO_2 can also occur as a clathrate in H_2O, acquiring two (and possibly three) different structures, depending on temperature and pressure at the time of condensation (Blake et al., 1991; Prasad et al., 2006), as well as the availability of other materials.

In all of these instances investigated in the laboratory,[2] the central wavelength and band profiles depend upon the nature of the association between the CO_2 molecules and their nearby molecular neighbors, and upon the instantaneous temperature as well as the temperature history of the sample. As noted in the Introduction, for the central wavelength of the asymmetric stretching mode in pure CO_2 ice at 80 K, we take 4.2675 μm (2343.3 cm^{-1}), rounded to 4.268 μm and 2343 cm^{-1}, from the laboratory work of Sandford and Allamandola (1990), and reference the following discussion to that value. Co-condensed mixtures of CO_2 and polar molecules (H_2O and CH_3OH) show variations in the strength, width, and central wavelength of the 4.268-μm band CO_2 band (Sandford and Allamandola, 1990; Ehrenfreund et al., 1999, and experiments conducted for the present work). As seen in nearly all of the binary and ternary mixtures examined by Sandford and Allamandola (1990) and Ehrenfreund et al. (1999) the band is shifted to longer wavelengths than pure CO_2, but Ehrenfreund et al. (their Fig. A1) found that a 1:1:1 mixture of CO_2, CH_3OH, and H_2O showed the band as unusually broad and with the center shifted to shorter wavelength. In their work, these properties of the band persisted over a temperature range 119–136 K. For the present paper, two of us (Mastrapa and Sandford) repeated spectroscopy of some of the same ternary mixtures and obtained results that corroborate those of Ehrenfreund et al. (1999).

Multi-component mixtures co-condensed at low temperature have the potential to take different structures, depending on the temperature and other conditions of the condensation. Amorphous solids, partially or fully crystalline, or clathrate structures are found. As the condensed material is heated, phase separations and microporous textures are found, as in the case of H_2O–CH_3OH ices (Blake et al., 1991), which were monitored by electron diffraction. Using this technique, Blake et al. (1991) identified the type II clathrate of CH_3OH trapped in H_2O cages. With a small quantity of CO_2 added to the mixture, its 4.268-μm C–O band broadened and shifted to 4.263 μm as some of the enclathrated CO_2 molecules were shifted to smaller (higher vibrational energy) sites upon warming of the mixture. Ehrenfreund et al. (1999) observed the

[2] Note on errors in laboratory data. All of the lab data shown here are infrared spectra obtained with Fourier transform spectrometers that integrate measurements of the target sample for a long enough time to obtain a signal precision (signal-to-noise) of at least 100, and typically ~500. Thus, random noise in the lab spectra is negligible for the present purpose. Also, the spectral resolution (defined as $\upsilon/\Delta\upsilon$) of such spectrometers is typically ~2300 or greater in the spectral region of the CO_2 band considered here. As noted in the text, the lab data were convolved to the lower dispersion of the VIMS data. This was done with a Gaussian function with $\sigma = 0.009$, resulting in $\lambda/\Delta\lambda$ ~255.

same behavior in similar ternary mixtures and in a binary mixture of H_2O and CO_2. As noted above, our experiments confirm this behavior, including the splitting of levels within the broadened and shifted CO_2 band (see Fig. 4). While CO_2 alone will form a clathrate with H_2O, the presence of a third molecule, CH_3OH in the cases noted, facilitates the formation of the clathrate structure, particularly at low pressures.

Prasad et al. (2006) observed by spectroscopy the formation of types I and II clathrates of CO_2 during thermal cycling of a fluid inclusion of CO_2 in a quartz vein in a rock specimen. The type II clathrate was seen at 93 K in the relatively high-pressure containment in the quartz, and upon warming the structure changed to type I and the specimen then melted. The spectra of Prasad et al. show structure in the band attributed to different energy levels in different structural sites. Figs. 4 and 5 show the Prasad spectrum at VIMS wavelength resolution. Its primary minimum is slightly longward of the Ehrenfreund spectral minimum, and clearly separated from the Blake clathrate.

Chaban et al. (2007) made *ab initio* calculations of several combinations of CO_2, H_2O, and CH_3OH. Their calculations of one CO_2 with two H_2O molecules fit the Prasad central wavelength, as well as the observational data for Hyperion's CO_2 band, which is representative of the broad and blue-shifted bands among the satellites of Saturn (Fig. 6).

4.2. Physisorbed and implanted CO_2 in non-ice materials

Hibbitts and Szanyi (2007) demonstrated in the laboratory that CO_2 physisorbed in zeolites and Ca-montmorillonite clay at cryogenic temperatures shows wavelength shifts consistent in some specific cases with the shifted CO_2 found on the Galilean satellites of Jupiter as well as the Saturn satellites discussed here. Zeolites, which are highly porous, can adsorb the non-polar CO_2 molecule because of the large number of isomorphic cation substitutions within the mineral structure, giving rise to local variations in the electrical field. These variations can induce charge imbalance in the CO_2 molecule, resulting in an attraction by the van der Waals force. Not all materials, even though porous, can effectively adsorb CO_2 because the effect depends on charge imbalances at various sites within the crystalline lattice of the host material.

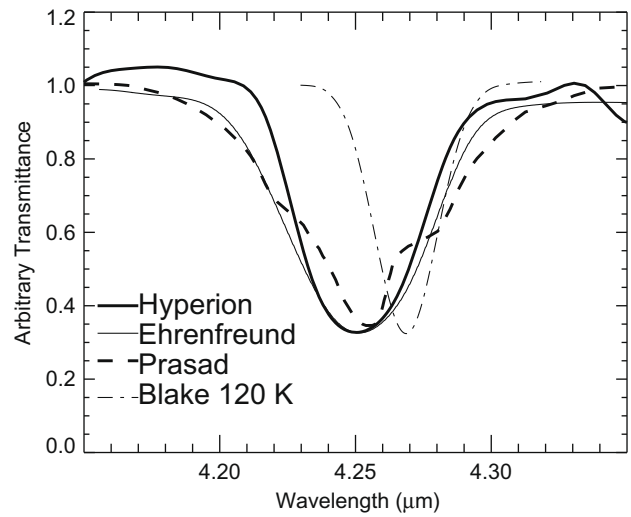

Fig. 5. The Hyperion CO_2 band in comparison with the Ehrenfreund et al. (1999) (see caption Fig. 4), the Blake et al. (1991) type II clathrate (see caption Fig. 3), and the Prasad et al. (2006) clathrate (see caption Fig. 4), all convolved to VIMS spectral resolution, $\lambda/\Delta\lambda = 255$. All of the laboratory data are transmission spectra.

The overall CO_2 absorption band strength and central wavelength depend on several factors, perhaps including temperature. The presence of multiple sites with differing electrical potentials within the host material effectively broadens the CO_2 band, and affects its symmetry. Hibbitts and Szanyi (2007) noted that the absorption band of CO_2 physisorbed on Ca-montmorillonite was centered at 4.258 μm, matching very closely the spectrum of CO_2 on the Galilean satellites observed with the Galileo Near-Infrared Mapping Spectrometer (NIMS), although the band shape was somewhat different.

Concerning implantation in ice, Strazzulla et al. (2003) have demonstrated that CO_2 is produced when carbon atoms (at energy 30 keV) are implanted in H_2O, noting that the subsequent destruction of CO_2 produces CO. They calculated that the abundance of CO_2 found on the Galilean satellites can be produced in the jovian environment on timescales of order 10^4–10^6 years.

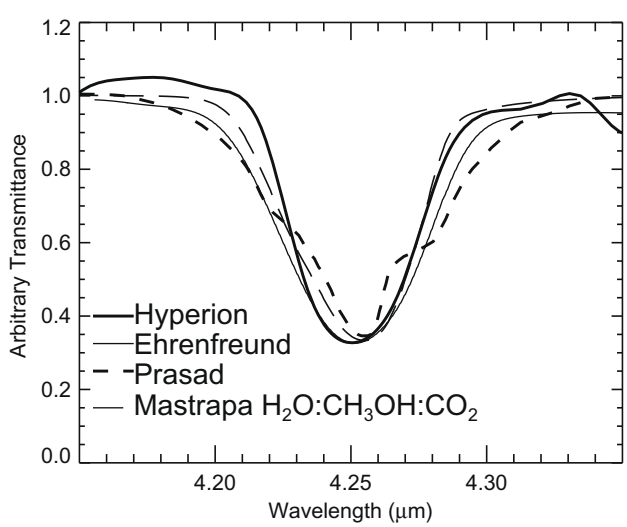

Fig. 4. The Hyperion CO_2 band is shown in comparison with the laboratory data of Ehrenfreund et al. (1999), Prasad et al. (2006), and Mastrapa and Sandford (obtained for this study). The Ehrenfreund et al. data represent a ternary mixture of H_2O, CO_2, and CH_3OH (proportions 1:1:1) at 121 K. All the laboratory data are transmission spectra and have been convolved to the VIMS spectral resolution, $\lambda/\Delta\lambda = 255$; see footnote to text.

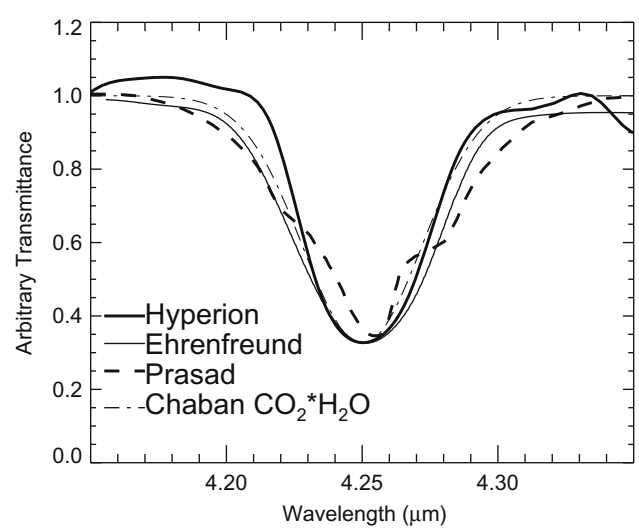

Fig. 6. Comparison of the Hyperion CO_2 band with the Prasad et al. (2006) laboratory spectrum and the Chaban calculated spectrum; the latter two have been convolved to the VIMS spectral resolution, $\lambda/\Delta\lambda = 255$.

4.3. Irradiation and shock production of CO_2

CO_2 is readily produced by the ion irradiation of ices containing O and C (Allamandola et al., 1988; Hudson and Moore, 1999; Palumbo et al., 1998; Baratta et al., 2007). Ehrenfreund et al. (1996) noted the production of CO_2 by the UV irradiation of CO embedded in H_2O ice. Once CO_2 and H_2O coexist, further radiation chemistry can occur through the interaction of magnetosphere charged particles (Delitsky and Lane, 2002), yielding several combinations of C, H, and O, including organic molecules. Implantation of N^+ and N_2^+ ions into a H_2O/CO_2 ice mixture can produce molecules with the C–N bond (e.g., HNCO, NCO, and R–OCN), after which the synthesis of amino acids is relatively straightforward. The prolific production of reactants in the ways described by Delitsky and Lane (2002), Benit et al. (1988), and Dello Russo et al. (1993) may account for the spectral diversity of Phoebe noted by Clark et al. (2005), although specific molecules in the reaction pathways have not yet been identified. See also the summary of laboratory work on irradiated ices by Strazzulla (1998).

CO_2 can also be formed by the ion irradiation of H_2O ice deposited on a refractory surface containing C (Mennella et al., 2004), and Ly-α irradiation of H_2O deposited on hydrogenated carbon grains (Mennella et al., 2006). Strazzulla and Moroz (2005) noted the production of CO_2 (measured wavelength 4.272 μm [2341 cm^{-1}]) by irradiating a sample of asphaltite (a solid bitumen) with a coating of H_2O ice (200 K) using 30 keV He^+ ions. Such carbonaceous materials arrive at the surfaces of the icy satellites from micrometeoritic material shed from comets.

The distances from Saturn of the four satellites considered here, expressed in Saturn radii (R_S) are: Dione 6.26, Hyperion 24.6, Iapetus 59.1, and Phoebe 215. All but Dione lie far from Saturn's equatorial ring current (inner and outer radii ~8 and ~16 R_S, respectively), and significant densities of trapped energetic ions and protons extend only about as far as 15 R_S (Krimigis et al., 1983). Hyperion and Iapetus receive 100 keV electron impacts and no significant protons, while at Phoebe's distance, the radiation environment from Saturn's magnetic field is very weak, and this outer satellite experiences radiation effects primarily from cosmic rays and solar UV flux. Johnson et al. (1983) have shown that CO_2 ice irradiated with energetic protons, such as cosmic rays, is chemically altered into CO and O_2, and is quickly lost to space at a rate significantly larger than the normal sublimation rate at a given temperature. While this loss process occurs on Phoebe in response to cosmic ray bombardment, it should be accelerated on those icy satellites within Saturn's proton-rich region (such as Dione in the present study). A quantitative study of CO_2 loss rates is beyond the scope of this paper.

Bibring and Rocard (1982) reported the laboratory synthesis of CO_2 in thin SiO_2 films by implantation of 40 keV $^{12}C^+$ ions, with the result that the CO_2 band thus formed has an approximately Gaussian profile with central frequency ~2340 cm^{-1} (λ = 4.274 μm). They compared this spectral feature with a band found in transmission spectra of lunar soil and conclude that CO_2 is formed in situ on the Moon by the implantation of C ions from the solar wind. Thus, implanted solar wind ions of H, C, and N react within the lunar grains to synthesize molecular compounds (Bibring et al., 1982).

CO_2 can also be generated by impact- or shock-induced chemistry from H_2O and a carbon source (such as CH_3OH; Nna-Mvondo et al., 2008).

All of these mechanisms are plausible to some degree in the Saturnian satellite system, and different mechanisms may dominate in specific geographical regions of specific satellites, depending upon the nature of the native materials and the local environment. We use the spectral data available to us to move toward an understanding of the dominant mechanisms on the four satellites discussed here.

5. Conclusions: nature and origin of CO_2 in Saturn's satellites

The possible origins of CO_2 in the Saturn satellite system can be summarized in outline form:

I. Native CO_2
- Original condensate in the solar nebula.
  - Amorphous mixture with other condensates.
  - CO_2 enclathrated in H_2O.

II. Non-native CO_2
- Radiation-produced.
  - UV and particle irradiation of ices containing sources of C and O.
  - UV and particle irradiation of refractory organic compounds in presence of H_2O.
  - Carbon ion addition to silicates or other source of O.
- Implantation
  - CO_2 implantation/deposition from external source.
  - Native CO_2 evaporated from subsurface and redeposited on surface.

The widespread (global) distribution of CO_2 on Phoebe, the primitive appearance of the body, and the characteristics of the band described above suggest that CO_2 on this satellite is a native component that has survived since condensation and accretion in its place of origin. Phoebe is thought to be a captured satellite, and it may have formed in the source region of Kuiper Belt objects. As such, its composition may be representative of a significant fraction of Kuiper Belt objects and short-period comets that emerge from the Kuiper Belt region. The volatility of CO_2 suggests that this molecule is currently being lost by evaporation, although enclathration of CO_2 in H_2O significantly lowers the vapor pressure. As we have noted, seen at the spectral resolution of VIMS the band width and wavelength are consistent with the Blake et al. (1991) type II clathrate, and if Phoebe's CO_2 is enclathrated, its long-term stability is enhanced.

The case has already been made for the hybrid nature of the CO_2 on the other three satellites considered here. Because CO_2 occurs in clear association with H_2O on Dione and Hyperion, it may originate in part from the irradiation of H_2O and a source of carbon, perhaps from micrometeorites. The irradiation source for tidally locked Dione is surely Saturn's magnetosphere, which sweeps past the satellite's trailing hemisphere, preferentially irradiating that region in contrast to the leading hemisphere. The leading-trailing asymmetry suggests that electrons, which have small gyroradii, are responsible for radiation effects, as opposed to ions, which have large gyroradii and for small bodies would affect the surface more nearly isotropically. Hyperion's rotation is not tidally locked and such magnetospheric irradiation effects as occur should be more or less globally isotropic. The low-albedo material in the cup craters of Hyperion may provide the local source of carbon needed to make CO_2.

In the case of Iapetus, the association of CO_2 with the low-albedo material (much of which also has a small amount of H_2O present) suggests that the CO_2 might originate by irradiation of the H_2O and the carbon locally available (Palmer and Brown, 2007).

Thus, in the VIMS spectral data for CO_2 in four satellites of Saturn, two basic patterns have emerged. Phoebe is the type example of the first pattern; seen at VIMS spectral resolution, the CO_2 band on Phoebe lies at the same wavelength as the laboratory data for pure CO_2 ice (Sandford and Allamandola, 1990) cited above, and has a profile of similar width when the laboratory data are convolved to the VIMS resolution. The same similarity occurs with the Blake et al. (1991) type II clathrate of CO_2 in H_2O.

The second pattern describes Hyperion, Dione, and the 2007 data for Iapetus; the CO_2 band is shifted to shorter wavelength and is significantly broader than the laboratory data for pure CO_2. The data for these three satellites are consistent with CO_2 complexed with other materials in such a way that the nearest neighbor molecules to the CO_2 are foreign. Whether they are another volatile, most likely H_2O, or a non-volatile material, cannot be established with certainty. In some instances, particularly Hyperion and Dione, the CO_2 is clearly associated with H_2O, as established from the compositional maps constructed from the VIMS data (for maps of Hyperion see Cruikshank et al., 2007; for Dione see Clark et al., 2008 and Stephan et al., in press). Clark et al. (submitted for publication) have demonstrated that CO_2 on Iapetus is variable in both strength and band central wavelength across the low-albedo region of this satellite.

The shifted and broadened CO_2 profiles seen on some satellites may originate from more than a single source, and they may also indicate the presence of a third, otherwise undetected molecule that has enabled the formation of a clathrate structure giving several different sites and energy states of the CO_2 molecule. Such multi-site trapping of CO_2 is suggested by the comparison to the Prasad et al. (2006) CO_2 clathrate and the ab initio calculations by Chaban et al. (2007) and shown in Figs. 4–6 above.

Limitations of the VIMS spectral resolution do not allow us to discriminate among the various molecular complexing scenarios noted above, but point to useful similarities to laboratory data obtained under various circumstances. Some degree of native CO_2 may appear in the spectrum, augmented by newly generated or mobilized CO_2 that is now complexed with other material(s).

Recognizing that *multiple* mechanisms for CO_2 production and distribution may account for its occurrence on the four satellites considered here, we summarize the conclusions of our work as follows:

1. Phoebe: the band shape and wavelength are consistent with pure CO_2 or the type II clathrate reported by Blake et al. (1991). Owing to its great distance from Saturn, trapped energetic particles in the planet's environment are unlikely to have a strong effect on the surface of Phoebe. Exposure to cosmic rays and solar UV is the main factor in removing or altering CO_2 on Phoebe.
2. Iapetus (2004 data): the band shape and wavelength are consistent with pure CO_2 or Blake's type II clathrate.
3. Iapetus (2007 data): the band shape is consistent with the Prasad clathrate and with calculated wavelengths of CO_2 lodged in multiple H_2O sites.
4. Hyperion: the band shape and wavelength are consistent with the Prasad clathrate, plus additional CO_2 lodged in multiple H_2O sites of various capacities.
5. The data are generally consistent with the complexing of CO_2 with non-volatile components of the surface, as has been proposed for Ganymede and Callisto.

The differences between the 2004 and 2007 data for Iapetus at first seem perplexing, but as noted in Section 3.2, Clark et al. (submitted for publication) have mapped the variability of CO_2 band strength and central wavelength across the surface of the satellite, showing that the amount and physical state of CO_2 is different at different locations. Work in progress by E. Palmer and R.H. Brown (private communication) will explore the distribution, state, and lifetime of CO_2 on Iapetus in greater detail.

In order to resolve open questions raised in this study, additional laboratory spectroscopy of clathrates of CO_2 in H_2O, with the structure verified by electron diffraction measurements made on the same sample, are important. Further evaluation of the role of a third kind of molecule on the formation of such clathrates would also be of interest. In terms of the observational data for Saturn's satellites, improved spectral resolution would be very valuable, but such measurements require an observing platform in space because of the opacity of the Earth's atmosphere in the region of the CO_2 band. A degree of spatial resolution on the satellites is also needed, since the CO_2 band is not distributed uniformly on any of the bodies discussed in this paper. There is no reasonable expectation of a return to the Saturn system with a spacecraft with such capability in the foreseeable future.

Acknowledgments

We thank the many people who designed and built the VIMS instrument and the Cassini spacecraft, as well as the engineers, managers, and scientists who have made the Cassini-Huygens mission a success of the highest magnitude.

Appendix A

The VIMS IR channel uses a linear array of 256 InSb detectors to produce IR spectra for each pixel in the FOV. The numbering scheme for the 256 wavelength increments (channels, or bands) used in this document begins with the shortest wavelength in the infrared component VIMS at 0.9498 μm designated 100, and the longest wavelength channel at 5.1225 μm designated 351 (motivated by IDL indexing starting at 0). The distribution of IR wavelengths on the array is quite linear, with detector central wavelengths spaced nominally on 16.7 nm intervals. Very slight second order effects in the spectrometer optics cause a small nonlinearity of order 20 nm, or about 0.5% over the total spectral range. Most of the residual deviations from nonlinearity, appearing as ripples of a few nm in Fig. 1 (Section 2), are due to imperfections in the wavelength setting mechanism of the source monochrometer used for the pre-launch calibration. Overall, nonlinearity of the wavelength scale is expected as a consequence of the triple blaze of the diffraction grating and the complex optical path of the instrument, as noted in Section 2.

Coauthor Meyer initially investigated the effect of telluric CO_2 absorption on VIMS detector wavelengths using a sequence of evenly spaced simple Gaussian profiles. These were convolved with a deep telluric CO_2 absorption profile, generated at 1 nm resolution with the atmosphere transmission program ATRAN (Lord, 1992). Meyer found that the resulting convolved profiles showed changes in their effective central wavelengths that were comparable to the large deviations from the linear fit described above. Once the actual detector spectral response measurements were inspected, Meyer concluded that the telluric CO_2 band was responsible for the distinctive wavelength deviations and pursued the further quantitative investigation and correction procedure that is described in this Appendix A.

In a parallel effort, coauthor Hibbitts has investigated the shape of the telluric CO_2 feature present in a VIMS radiometric calibration spectrum. This continuum spectrum was originally obtained as part of the VIMS absolute radiometric calibration in July 1996 (see Fig. A1, top). A moderately deep unsaturated telluric CO_2 absorption is evident in this spectrum.

The continuum beyond 3 μm was from the local thermal background emission (not the blackbody test source), but is well fitted by a 310 K blackbody spectrum, scaled with a fixed emissivity factor. After dividing the VIMS spectrum by this thermal continuum spectrum, the telluric CO_2 absorption feature appears to have a minimum transmission of about 75% (see Fig. A1, bottom). For comparison to a model, an atmosphere CO_2 absorbance profile at 1 cm^{-1} resolution was obtained from the DOE/PNNL Infrared Spectral Library Release 13b, January, 2008 (see Sharpe et al., 2004, and

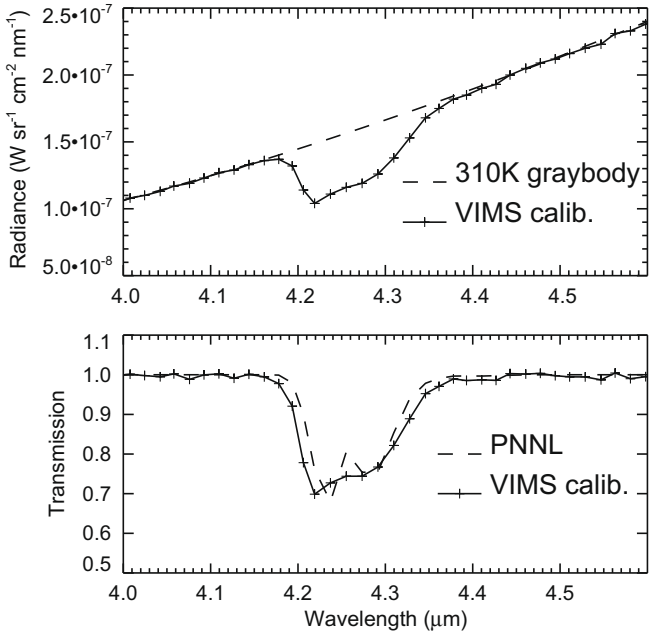

Fig. A1. (Upper): VIMS radiometric calibration spectrum showing CO_2 absorption feature at 4.3 μm, overlaid with fitted thermal continuum. (Lower): transmission spectrum from ratio, compared to CO_2 atmosphere model convolved to VIMS resolution and RC15 baseline wavelengths.

http://secure2.pnl.gov/nsd/nsf/Welcome), and scaled to 1 ppm over a 1 meter path.[3] This was re-sampled to VIMS resolution, with the result also shown in the lower plot of Fig. A1. The differences between the observed and calculated profile suggested that better agreement might occur if several of the points in the observed VIMS ground calibration profile were shifted to the right by various amounts. The observed absorption profile was found to match the model absorption profile by shifting the effective wavelengths of bands 296–305 (see Fig. A2). This was done by shifting the center band (300) by +7 nm, and the others by smaller values decreasing to +1 or +2 nm at the outermost bands 296 and 305.

It was also found that using these modified wavelength values for these bands made the VIMS observed spectrum of CO_2 ice on Callisto agree with the Galileo NIMS spectrum of the same feature. This separate investigation of the distorted shape of the telluric CO_2 absorption profile in the VIMS radiometric calibration provided independent evidence that the ground calibration of the VIMS wavelength scale was probably affected by telluric absorption.

The original 1996 pre-launch VIMS wavelength calibration data was made available to Meyer by Clark in early 2007. Strong telluric CO_2 absorption is clearly evident in the sequence of profiles, with peak signals near 4.2 μm attenuated down to only a few percent of typical peak values outside the telluric CO_2 absorption feature (see Fig. A3).

A more authentic simulation was performed, using a re-created sequence of detector response profiles spanning the affected wavelength range, based on unaffected profiles. First a single template profile was created by combining the measured response profiles for bands 281 through 292 (3.95–4.13 μm). Copies of this template profile were positioned at fixed spacing of 16.8 nm, and with slowly dropping peak heights based on the trend for the unaffected

[3] The selected pathlength and abundance gives a model spectrum that closely matches the appearance of the CO_2 band seen in the actual VIMS calibration data (Fig. A3) in terms of the height of the central peak between the P and R branches, and the non-zero intensity at the bottoms of the branches.

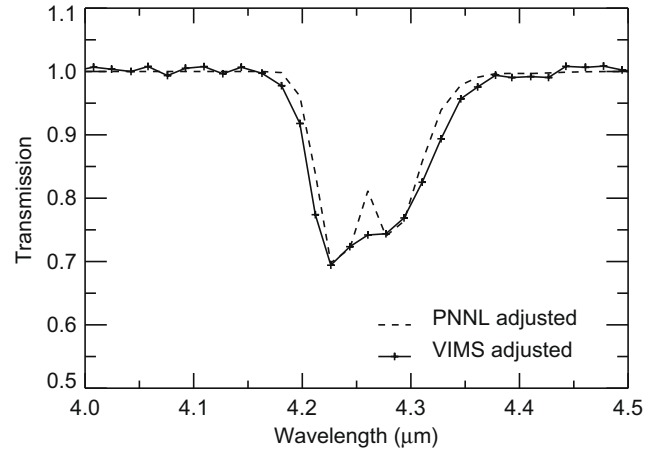

Fig. A2. CO_2 profile after wavelength adjustments, compared to model.

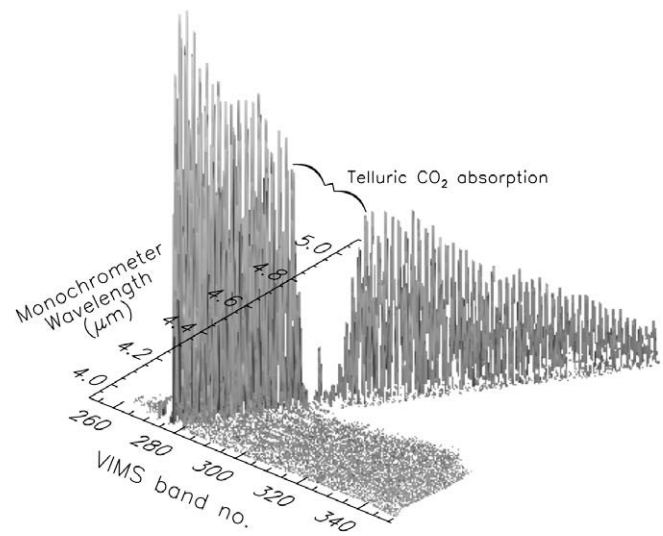

Fig. A3. VIMS wavelength calibration spectra for ~4 to 5 μm. The region affected by telluric CO_2 absorption is marked.

profiles outside the affected interval. This was assumed to be a reasonable approximation for profiles that would have been obtained if there had been no CO_2 in the calibration light path. This simulated "vacuum profile sequence" was then convolved with the same telluric transmission curve used earlier for the preliminary simulation. The vacuum profile sequence, and the ATRAN atmospheric transmission curve before they were convolved are shown in Fig. A4.

The result of the convolution, and the actual measured band profiles in the affected wavelength range, are shown in Fig. A5 for comparison. The relative strengths and apparent positions of the simulated convolved profiles appear to be quite similar to the actual measured band profiles, and the resulting position deviations are similar to those for the current baseline wavelength list.

The effect of the convolution on the apparent positions of the profiles is also shown by shifting them into superposition, using displacements equal to their original spacing before convolution. This is shown in Fig. A6 for bands 293–301. The expected effect of the atmospheric transmission gradient is evident, reducing the red side of the profiles for bands 296–299 such that their apparent positions are shifted increasingly to shorter wavelength.

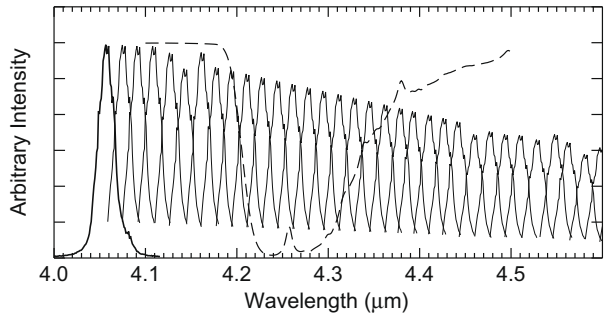

Fig. A4. Sequence of copies of a template profile (the bold profile on the left is the type example), positioned at either the current baseline RC15 wavelength values, or on a sequence of fixed spacing positions where telluric CO_2 may have had some effect. The heights for these were set by linear interpolation from the general trend of unaffected measured profiles. The model atmosphere transmission from ATRAN is shown as a dashed line.

The inverse of the convolution process was performed by dividing the actual calibration profiles by the same telluric CO_2 transmission curve used above. This should produce an approximate cancelation of the distortions and shifts of the affected profiles caused by the shape and depth of the telluric CO_2 absorption. This was done using the calibration data for 20 bands containing the affected wavelength range. The result is shown in Fig. A7.

Although the most strongly attenuated signals were very weak and noisy compared to their unaffected neighbors, the resulting "corrected" profiles have more uniform spacing and shapes. Fig. A7 includes simple Gaussian peaks least squares fitted to these "corrected" profile data sets for each of the detectors. Deviations from Eq. (1), the global baseline linear fit to the current wavelength list, were calculated for the central wavelengths of these Gaussian fits to the 20 corrected profiles.

The deviations from the global baseline linear fit are plotted in Fig. A8 for:

(a) the RC15 baseline wavelength list currently in use;
(b) the wavelengths re-determined here from the original calibration data;
(c) the wavelengths for the profiles for 20 bands after deconvolution.

Outside the interval evidently affected by telluric CO_2, the pattern of deviations for (b) and (c) are effectively identical to those for the baseline RC15. The deviations for (b) within the affected interval show the growing blueward (negative) shift as the bands step into the CO_2 absorption. Similarly the deviations become noticeably positive (redward) for bands 301–305, as their red sides

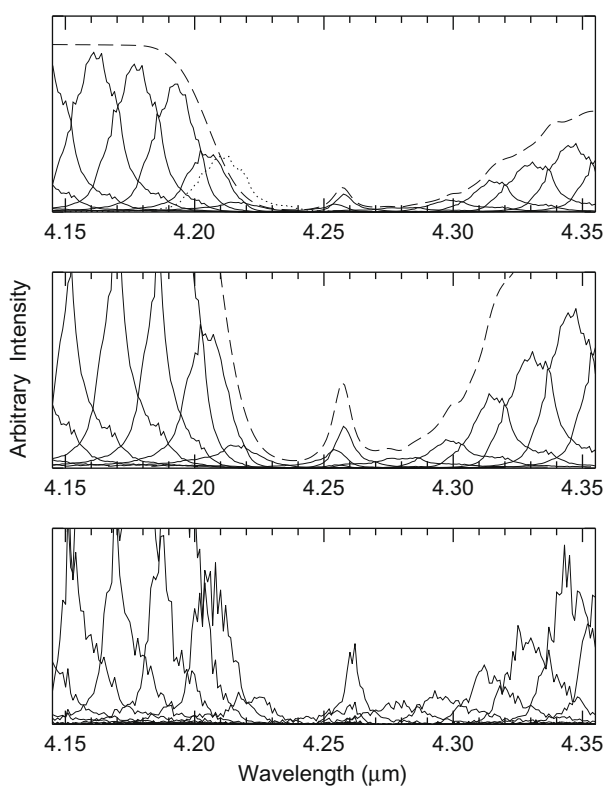

Fig. A5. (Top): profile sequence in the range 4.15–4.35 μm, after convolution with the CO_2 transmission curve (dashed line). A copy of the template profile at the initial position used for band 298 before convolution is shown as a dotted line, scaled down to the same height as the convolved result. (Middle): vertically stretched version of the upper plot, to make the shapes of the most severely attenuated profiles more readily visible. (Bottom): actual calibration profiles in this wavelength range, plotted with a *y*-axis range chosen for comparison to the middle plot. Note the similarity of the locations, relative heights, and general shapes of the affected profiles from 4200 nm through 4350 nm.

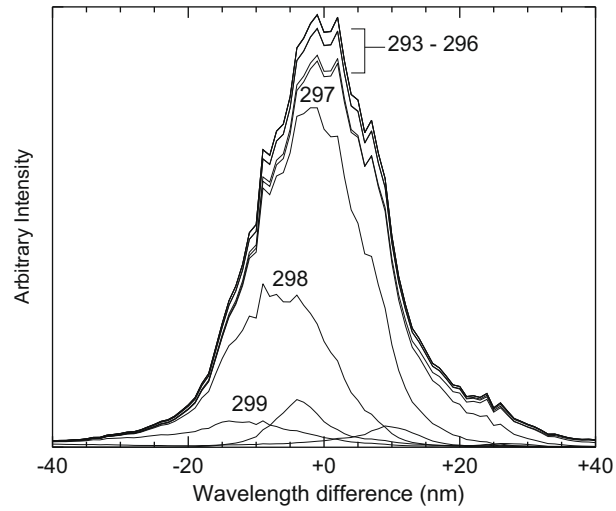

Fig. A6. Superposition of several template profiles after convolution with the transmission curve, and then shifted by their original wavelength difference from band 293. Bands 297–299 are deep in the blue wing of the telluric CO_2 absorption, and the convolved profiles show the bias in their apparent locations introduced by the gradient of the transmission. The convolved profile for band 298 appears to have moved about 8 nm to the left from its original position.

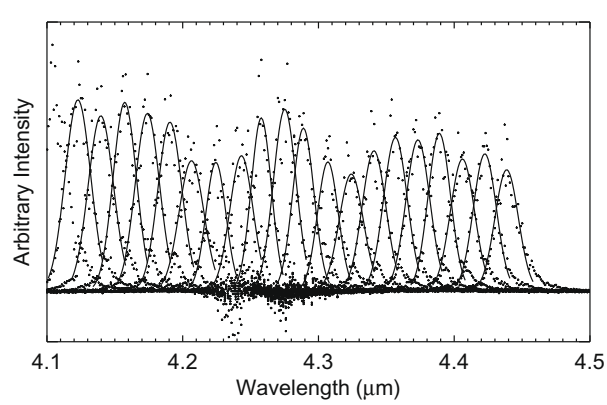

Fig. A7. Wavelength calibration data in the range 4.1–4.45 μm after division by the CO_2 transmission curve. Each band profile is the average of four separate spectra. The highly attenuated and shifted profiles around 4.3 μm are now roughly evenly spaced and similar in height to the adjacent unaffected profiles.

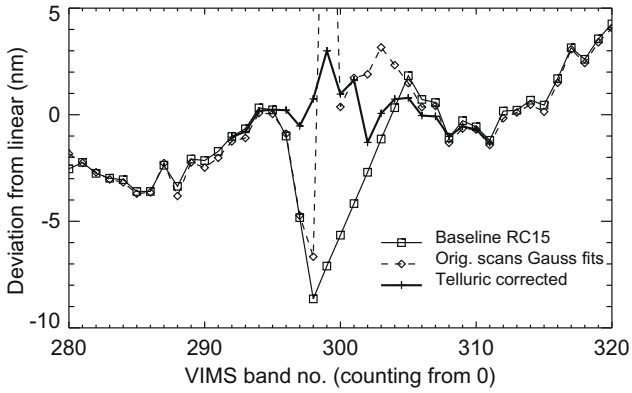

Fig. A8. Deviations (in nm) from Eq. (1) for the RC 15 wavelength calibration, the original response profiles data, and 20 of these same profiles after correcting for telluric absorption.

(including the intrinsic extended red wing) get over-weighted where the transmission is rising back up. Bands 299 and 300 show extreme deviations where the Gaussian fits were dominated by signal from the wings of those bands through the central peak in the transmission curve.

The deviations from Eq. (1) for the corrected profiles are only about −1 to +3 nm, and perhaps would be within about 0 to +2 nm if the data were less noisy. Given the overall appearance of the deviations outside the affected interval, the corrected deviations might be expected to fall on a smoother curve, probably slightly convex upward. A sequence of deviations chosen to have this character is shown in Fig. A9. Adding these deviations to Eq. (1) for the corresponding bands produces alternative values of the wavelengths, which are based primarily on the outcome of dividing the original calibration data by the model telluric CO_2 transmission curve. The replacement wavelengths for bands 295–307 are listed in Table 2 in Section 2.

Unless the data are subjected to more detailed analysis, noise filtering, error analysis, etc. there may remain some uncertainty as to whether the new wavelengths are the best possible replacement. Table 2 includes the RC15 baseline wavelength values, their deviations (in nm) from the linear fit of Eq. (1), and for comparison the deviations from Eq. (1) for three alternatives. These include a local linear "bridge" across the top of the "V" shape of the RC15 deviations, a quadratic (2nd order) fit to RC15, and the deviations for the smooth curve described above and shown in Fig. A9. The latter is labeled "Deconv. smooth" in Table 2, to indicate this is the smoothed version of the result of deconvolving telluric transmission from actual measured detector profiles, as described above.

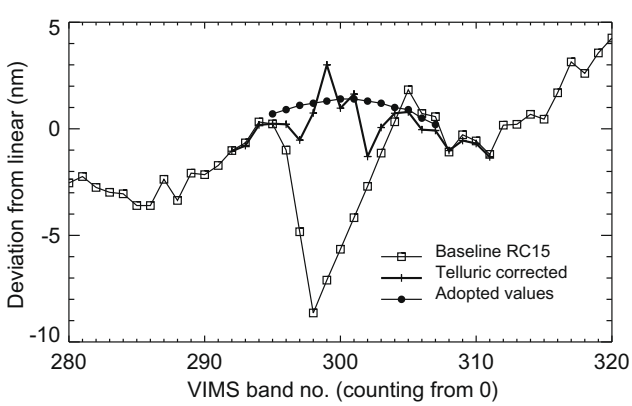

Fig. A9. Deviations for RC15, and for profile data corrected for telluric absorption. The smooth curve of deviations is also shown (large dots). The latter added to Eq. (1) produce the new wavelength assignments in this interval, listed in Table 2.

Note that all of the alternatives differ from each other by less than 2 nm, which is small compared to the 5 nm amplitude of the periodic pattern evident in Fig. 1, and this pattern as noted earlier has been described as an artifact of the calibration monochrometer. From this perspective, using any of the alternatives listed (other than the current RC15 baseline) would provide effectively about the same "repair" for the affected wavelength interval, and eliminate the distortion of spectra in this region due to using the baseline values. Since the "new" column is based on actual calibration data with the evident telluric absorption effect substantially divided out, and those results appear to be reasonably consistent with the overall character of RC15 elsewhere, this is formally the preferable alternative.

References

Allamandola, L.J., Sandford, S.A., Valero, G.J., 1988. Photochemical and thermal evolution of interstellar/precometary ice analogs. Icarus 76, 225–252.

Baratta, G.A., Brunetto, R., Caniglia, G., Fulvio, D., Ioppolo, S., Leto, G., Palumbo, M.E., Spinella, F., Strazzulla, G., 2007. Ion irradiation of TNO surface analogue ice mixtures: The chemistry. Mem. Soc. Astron. It. 11 (Suppl.), 185–189.

Benit, J., Bibring, J.P., Rocard, F., 1988. Chemical irradiation effects in ices. Nucl. Instrum. Methods Phys. Res. B32, 349.

Bibring, J.-P., Rocard, F., 1982. Ion implantation phenomena in space. Radiat. Eff. 65, 159–165.

Bibring, J.-P., Langevin, Y., Rocard, F., 1982. Synthesis of molecules by irradiation in silicates. in: Proc. 13th Lunar Planet. Sci., Conf., J. Geophys. Res. 87 (Suppl.), A446–A450.

Blake, D.F., Allamandola, L.J., Sandford, S.A., Hudgins, D., Freund, F., 1991. Clathrate hydrate formation in amorphous cometary ice analogs in vacuo. Science 254, 548–551.

Brown, R.H., and 22 colleagues, 2004. The Cassini visual and infrared mapping spectrometer investigation. Space Sci. Rev. 115, 111–168 (Cassini issue).

Brown, R.H., and 25 colleagues, 2005. Observations in the Saturn system during approach and orbital insertion, with Cassini's Visual and Infrared Mapping Spectrometer (VIMS) 2006. Astron. Astrophys. 446, 706–716.

Buratti, B.J., Cruikshank, D.P., and the VIMS Team, 2005. *Cassini* visual and infrared mapping spectrometer observations of Iapetus: Detection of CO_2. Astrophys. J. 622, L149–L152.

Chaban, G.M., Bernstein, M., Cruikshank, D.P., 2007. Carbon dioxide on planetary bodies: Theoretical and experimental studies of molecular complexes. Icarus 187, 592–599.

Clark, R.N., and 25 colleagues, 2005. Compositional mapping of Saturn's moon Phoebe with imaging spectroscopy. Nature 435, 66–69.

Clark, R.N., and 11 colleagues, 2008. Compositional mapping of Saturn's satellite Dione with Cassini VIMS and the implications of dark material in the Saturn system. Icarus 193, 372–386.

Clark, R.N., and 10 colleagues, 2009. The composition of Iapetus: Mapping results from Cassini VIMS. Icarus, submitted for publication.

Coradini, A., and 33 colleagues, 2008. Identification of spectral units on Phoebe. Icarus 193, 233–251.

Cruikshank, D.P., Dalton, J.B., Dalle Ore, C., Bauer, J., Stephan, K., and the *Cassini* VIMS and UVS Teams, 2007. Surface composition of Hyperion. Nature 448, 54–56.

Cruikshank, D.P., Roush, T.L., Owen, T.C., Geballe, T.R., de Bergh, C., Schmitt, B., Brown, R.H., Bartholomew, M.J., 1993. Ices on the surface of Triton. Science 261, 742–745.

Delitsky, M.L., Lane, A.L., 2002. Saturn's inner satellites: Ice chemistry and magnetosphere effects. J. Geophys. Res. 107 (E11), 5093.

Dello Russo, N., Khanna, R.K., Moore, M.H., 1993. Identification and yield of carbonic acid and formaldehyde in irradiated ices. J. Geophys. Res. 98, 5505–5510.

Ehrenfreund, P., Boogert, A.C.A., Gerakines, P.A., Jansen, D.J., Schutte, W.A., Tielens, A.G.G.M., van Dishoeck, E.F., 1996. A laboratory database of solid CO and CO_2 for ISO. Astron. Astrophys. 315, L341–L344.

Ehrenfreund, P., Kerkhov, O., Schutte, W.A., Boogert, A.C.A., Gerakines, P.A., Dartois, E., d'Hendecourt, L., Tielens, A.G.G.M., van Dishoeck, E.F., Whittet, D.C.B., 1999. Laboratory studies of thermally processed H_2O–CH_3OH–CO_2 ice mixtures and their astrophysical implications. Astron. Astrophys. 350, 240–253.

Estrada, P., Mosqueira, I., Lissauer, J., D'Angelo, G., Cruikshank, D., 2009. Formation of Jupiter and conditions for accretion of the Galilean satellites. In: Pappalardo, R.T., McKinnon, W.B., Khurana, K. (Eds.), Europa. Univ. Arizona Press.

Gavrishin, A.I., Coradini, A., Cerroni, P., 1992. Multivariate classification methods in planetary sciences. Earth Moon Planets 59, 141–152.

Gerakines, P.A., and 10 colleagues, 1999. Observations of solid carbon dioxide in molecular clouds with the Infrared Space Observatory. Astrophys. J. 522, 357–377.

Grundy, W.M., Young, L.A., Speancer, J.R., Johnson, R.E., Young, E.F., Buie, M.W., 2006. Distributions of H_2O and CO_2 ices on Ariel, Umbriel, Titania, and Oberon from IRTF/SpeX observations. Icarus 184, 543–555.

Hibbitts, C.A., Klemaszewski, J.E., McCord, T.B., Hansen, G.B., Greeley, R., 2002. CO_2-rich impact craters on Callisto. J. Geophys. Res. 107 (E10), 14-1–12.
Hibbitts, C.A., Pappalardo, R.T., Hansen, G.B., McCord, T.B., 2003. Carbon dioxide on Ganymede. J. Geophys. Res. 108 (E5), 2-1–22.
Hibbitts, C.A., Szanyi, J., 2007. Physisorption of CO_2 on non-ice materials relevant to icy satellites. Icarus 191, 371–380.
Hibbitts, C.A., McCord, T.B., Hansen, G.B., 2000. Distributions of CO_2 and SO_2 on the surface of Callisto. J. Geophys. Res. 105 (E9), 541–557.
Hudson, R.L., Moore, M.H., 1999. Laboratory studies of the formation of methanol and other organic molecules by water + carbon monoxide radiolysis: Relevance to comets, icy satellites, and interstellar ices. Icarus 140, 451–461.
Jaumann, R., and 28 colleagues, 2006. High-resolution Cassini-VIMS mosaics of Titan and the icy saturnian satellites. Planet. Space Sci. 54, 1146–1155.
Johnson, R.E., Lanzerotti, L.J., Brown, W.L., Augustyniak, W.M., Mussil, C., 1983. Charged particle erosion of frozen volatiles in ice grains and comets. Astron. Astrophys. 123, 343–346.
Krimigis, S.M., Carbary, J.F., Keath, E.P., Armstrong, T.P., Lanzerotti, L.J., Gloeckler, G., 1983. General characteristics of hot plasma and energetic particles in the saturnian magnetosphere. Results from the Voyager spacecraft. J. Geophys. Res. 88, 8871–8892.
Lebofsky, L.A., 1975. Stability of frosts in the Solar System. Icarus 25, 205–217.
Lord, S.D., 1992. NASA Tech. Mem. 103957.
McCord, T.B., and 13 colleagues, 1998. Non-water–ice constituents in the surface material of the icy Galilean satellites from the Galileo near-infrared mapping spectrometer investigation. J. Geophys. Res. 103 (E4), 8603–8626.
McCord, T.B., and 24 colleagues, 2004. Cassini VIMS observations of the Galilean satellites including the VIMS calibration procedure. Icarus 172, 104–126.
Mennella, V., Palumbo, M.E., Baratta, G.A., 2004. Formation of CO and CO_2 molecules by ion irradiation of water ice-covered hydrogenated carbon grains. Astrophys. J. 615, 1073–1080.
Mennella, V., Baratta, G.A., Palumbo, M.E., Bergin, E.A., 2006. Synthesis of CO and CO_2 molecules by UV irradiation of water ice-covered hydrogenated carbon grains. Astrophys. J. 643, 923–931.
Nna-Mvondo, D., Khare, B., Ishihara, T., McKay, C.P., 2008. Experimental impact shock chemistry on planetary icy satellites. Icarus 194, 822–835.
Palmer, E.E., Brown, R.H., 2006. Carbon dioxide transport on Iapetus. LPI Abstract 2215.
Palmer, E.E., Brown, R.H., 2007. A possible trace carbon dioxide polar cap on Iapetus. Astrophys. J. Lett. 666, L125–L128.
Palmer, E.E., Brown, R.H., 2008. The stability and transport of carbon dioxide on Iapetus. Icarus 195, 434–446.
Palumbo, M.E., Baratta, G.A., Brucato, J.R., Castorina, A.C., Satorre, M.A., Strazzulla, G., 1998. Profile of the CO_2 bands produced after ion irradiation of ice mixtures. Astron. Astrophys. 334, 247–252.
Prasad, P.S.R., Shiva Prasad, K., Thakur, N.K., 2006. FTIR signatures of type-II clathrates of carbon dioxide in natural quartz veins. Curr. Sci. 90, 1544–1547.
Sandford, S.A., Allamandola, L.J., 1990. The physical and infrared spectral properties of CO_2 in astrophysical ice analogs. Astrophys. J. 355, 357–372.
Sharpe, S.W., Johnson, T.J., Sams, R.L., Chu, P.M., Rhoderick, G.C., Johnson, P.A., 2004. Gas-phase databases for quantitative infrared spectroscopy. Appl. Spectrosc. 58, 1452–1461.
Stephan, K., and 12 colleagues, in press. Dione's spectral and geological properties. Icarus. 206, 631–652.
Strazzulla, G., 1998. Chemistry of ice induced by bombardment with energetic charged particles. In: Schmitt, B., de Bergh, C., Festou, M. (Eds.), Solar system ices. Kluwer Academic Publishers, pp. 281–301.
Strazzulla, G., Moroz, L., 2005. Ion irradiation of asphaltite as an analogue of solid hydrocarbons in the interstellar medium. Astron. Astrophys. 434, 593–598.
Strazzulla, G., Leto, G., Gomis, O., Satorre, M.A., 2003. Implantation of carbon and nitrogen ions in water ice. Icarus 164, 163–169.
Thomas, P., and 17 colleagues, 2007. Hyperion's sponge-like appearance. Nature 448, 50–56.